International Journal for Housing Science and Its Applications
Publish August 10, 2025. Volume 46, Issue 4 Pages 4999-5009

https://doi.org/10.70517/ijhsa464343

Analysis of the spatio-temporal characteristics of plateau vortex-atmospheric circulation coupling based on adaptive filtering

Jinpeng Yue[1,*]
[1] School of Earth and Environment, University of Leeds, Leeds, LS2 9JT, UK
Corresponding authors: (e-mail: jpy2478099379@163.com).

Abstract The coupling effect between plateau eddies and atmospheric circulation has important impacts on climate change and weather systems, especially in the Tibetan Plateau region. Due to the uniqueness of the region's topography, the interactions with the atmospheric circulation during the generation, development and extinction of eddies are complicated. In this paper, the spatial and temporal characteristics of the coupling effect of plateau eddies with atmospheric circulation are investigated by using three sets of high-resolution reanalysis data (MERRA-2, ERA-Interim, and JRA55), as well as satellite observations, combined with the objective identification method of plateau eddies, atmospheric heat source calculation, and the LMS adaptive filtering algorithm. The results show that there is a significant difference in the number of generated plateau vortices between 1985 and 2018, with 22 in 1985 and 7 in 2018. The surface sensible heat fluxes were significantly different between the more and less generating years, 77.4 W/m² in 1985 and 74.3 W/m² in 2018. In addition, the interannual variations of plateau vortex generation and its seasonal characteristics in the three data sets also showed significant periodicity and geographical differences. It was further found that the surface heat source, sensible heat and latent heat are significantly linked to the generation of plateau vortex and atmospheric circulation, especially during the warm season when the interaction between the surface heat source and atmospheric circulation is more closely related.

Index Terms Plateau vortex, atmospheric circulation, spatial and temporal characteristics, LMS algorithm, heat source, sensible heat

I. Introduction

China's topography is high in the west and low in the east, and many plateaus, mountains, and plains form the "three-tiered" terrain of Chinese mainland [1]. The main body of the Qinghai-Tibet Plateau is located in the first of China's three major tiered terrains, and is known as the "Roof of the World", "Atmospheric Water Tower", and "The Third Pole of the World" [2]. On the one hand, forced by the topography of the main body of the Tibetan Plateau and the surrounding mountain systems, the low-level westerly airflow branches out on the west side of the plateau and converges on the east side of the plateau after circling around from the north and south, and forms constant positive and negative vorticity bands on the north and south sides of the plateau, i.e., the small high-pressure of Nanjian and Lanzhou on the north side of the plateau, and the southwestern vortex and so on on on the east side of the plateau [3]-[6]. This is similar to the formation process of vorticity pairs on the back side of the cylinder in the experiment of water flow over a cylindrical model [7]. On the other hand, the bypassing and climbing motions of the westerly jet contribute decisively to the formation of the mean field of the winter atmospheric circulation in East Asia [8], [9]. For example, tropical oceanic water vapor is transported around the plateau to mid- and high-latitudes to enhance the East Asian summer winds, while the summer convective system over the Tibetan Plateau often moves eastward out of the plateau leading to heavy precipitation in the downstream basin [10]-[12]. Based on this, the convective sources of the Tibetan Plateau orography profoundly affect the weather and climate change as well as the moisture cycle in China and the whole world [13], [14]. Exploring the coupling effect of plateau eddies and atmospheric circulation in the Tibetan Plateau Large Terrain will be helpful to understand the changing characteristics of the plateau bypassing effect in winter and spring, and thus deepen the understanding of weather and climate.

In this paper, firstly, the vortex feature points are extracted by the objective identification method of the plateau vortex, and then the spatio-temporal evolution of the plateau vortex is tracked using the DBSCAN clustering algorithm. Secondly, the relationship between plateau vortices and atmospheric heat sources is analyzed using the LMS adaptive filtering algorithm, and their influence on the generation of plateau vortices is explored by calculating the surface heat sources, sensible and latent heat fluxes on the Tibetan Plateau. Finally, the coupling characteristics of the plateau vortex activity with the atmospheric heat source and atmospheric circulation are revealed by comparing with the atmospheric circulation characteristics. The innovation of this study is to reveal the coupling effect between the plateau vortex and the atmospheric circulation through the adaptive filtering method, which further clarifies the relationship between the surface heat source and the vortex generation. At the same time, this paper selects high resolution climate data from multiple sources to comprehensively analyze the spatial and temporal changes of the plateau vortex, which provides an important theoretical basis for an in-depth understanding of the climate change on the Qinghai-Tibetan Plateau.

II. Sources of information for the study

In order to study the spatial and temporal characteristics of the coupled effects of the plateau vortex and atmospheric circulation, and to avoid the uncertainty caused by the use of a single set of data, this paper selects three sets of reanalysis data with high spatial and temporal resolution (MERRA-2, ERA-Interim, and JRA55, which use the time period of 1985-2018) that have a better simulation capability in the Tibetan Plateau, as well as the data of cloud-top brightening and precipitation based on satellite observations to carry out the study. The study is carried out based on satellite observations of cloud-top brightness and precipitation data.

In addition, this paper uses the 1998-2021 “Yearbook of Low Vortices and Shear Lines over the Tibetan Plateau” (the “Yearbook”) data compiled by the Chengdu Institute of Plateau Meteorology (CIPM), as well as the GPM-starable precipitation and cloud-top brightness temperatures, to validate the plateau vortices obtained by the objective identification method. In this paper, we use CN05.1 data to calculate the daily mean temperature, daily maximum temperature, daily minimum temperature, and daily difference in temperature over the Tibetan Plateau.

III. Research methodology

In this study on the spatial and temporal characteristics of the coupling effect of plateau vortex and atmospheric circulation, this paper adopts the identification method of plateau vortex object, the calculation method of atmospheric heat source and the LMS adaptive filtering algorithm to carry out the study.

III. A. Plateau vortex objective identification method

The objective identification of plateau vortices is carried out in three steps.

(1) Plateau vortex feature point extraction

Within the encompassing area of the Tibetan Plateau and its surrounding areas (17. 5°N-47.5°N, 72-5°E-122-5°CE), after smoothing the geopotential height, zonal wind and meridional wind at nine points, traverse all the grid points in the study area from north to south and from west to east, if the traversed grid points satisfy: the wind direction in the range of 5°×5° around a point satisfies the counterclockwise rotation, that is, the average zonal wind speed on the south side is greater than 0, the average zonal wind speed on the north side is less than 0, the average meridional wind speed on the east side is greater than 0, and the average meridional wind speed on the west side is less than 0, If the geopotential height value of the grid point is less than and the relative vorticity value is greater than the average value of the surrounding area of 5°×5°, the grid point is considered to be the characteristic point of the plateau vortex.

(2) Identify the plateau vortex center

The latitude and longitude of the plateau vortex center were determined by using the DBSCAN clustering algorithm to cluster the plateau vortex feature points obtained in step 1) [15]. After repeated tests, the neighborhood radius and the minimum number of neighborhood points in the DBSCAN algorithm are taken as 1.0 and 10.0, respectively.

(3) Plateau vortex tracking

On the basis of step 2), for two adjacent time periods $t, t+1$ (i.e., assuming that the plateau vortex life history ≥ 12h), if there are plateau vortices and the distance between the centers of the plateau vortices of the two adjacent time periods ≤ 300km, the two plateau vortices are regarded as the same plateau vortex moving at different moments, otherwise they are regarded as different moments of the plateau vortex; and then analogous to the moments of $t+2$, the number of plateau vortices generated and the moving trajectories of plateau vortices can be obtained. In this paper, the intensity of plateau vortex is defined as the average value of relative vorticity, cumulative precipitation, and cloud-top brightness temperature of ≤220 K within the range of 5°×5° from the center of plateau vortex during the whole life history period. Repeatedly performing the above three steps, the characteristics of generated and removed plateau vortices during the study period can be obtained, where the removed plateau vortices are included in the generated plateau vortices.

III. B. Calculation methods for atmospheric heat sources

In order to analyze the relationship between changes in plateau eddy activity and the heat source on the Tibetan Plateau, this paper uses an inverse algorithm to calculate the atmospheric heat source on the Tibetan Plateau:

$$Q_1 = c_p \left(\frac{p}{p_0} \right)^k \left(\frac{\partial \theta}{\partial t} + \vec{V} \cdot \nabla \theta + \omega \frac{\partial \theta}{\partial p} \right) \tag{1}$$

$$Q_2 = -L \left(\frac{\partial q}{\partial t} + \vec{V} \cdot \nabla q + \omega \frac{\partial q}{\partial p} \right) \tag{2}$$

$$\langle Q_1 \rangle = -\frac{1}{g} \int_{p_s}^{p_s} Q_1 dp \tag{3}$$

$$\langle Q_2 \rangle = -\frac{1}{g} \int_{p_s}^{p_s} Q_2 dp \tag{4}$$

where, Q_1, Q_2 denote the atmospheric apparent heat source and apparent water vapor sink for each isobaric surface layer, respectively; $\langle Q_1 \rangle, \langle Q_2 \rangle$ denotes the apparent heat source and apparent water vapor sink of the whole atmosphere, respectively; c_p is the specific heat (in J·K^{-1}·kg^{-1}) at constant pressure; p is air pressure (in Pa); p_0 is a constant, taken as 1000hPa; κ is a constant, taken as 0.286; θ is the bit temperature (in K); t is the integration time (in s); The $\vec{V}$ is the horizontal velocity vector (in m·s^{-1}); ∇ is the horizontal gradient operator; ω is the vertical velocity (in Pa·s^{-1}); L is the latent heat of condensation at zero degrees Celsius (unit: J·kg^{-1}); q is the specific humidity (in kg·kg^{-1}); g is the acceleration of gravity, taken as 9.8 m·s^{-2}; p_s represents the surface pressure; p_t represents the top-of-atmosphere pressure, taken as 200 hPa.

III. C. LMS Adaptive Filtering Algorithm

III. C. 1) Algorithmic principles

The LMS algorithm uses the most rapid gradient descent method to search for the optimal value based on Wiener filtering [16], [17]. When the adaptive filter iterates step by step, the LMS algorithm searches in the negative direction of the estimated gradient, and the accuracy of the gradient value estimation directly determines the accuracy of the LMS algorithm during the search process. When the step size of the algorithm is unreasonable, the gradient value required for each iteration cannot be estimated accurately, and the weight coefficients of the filter cannot converge to the Wiener solution. Since one of the drawbacks of Wiener filtering is the need to know the a priori knowledge, the a priori knowledge is almost impossible to obtain in practice. Therefore, the instantaneous error quadratic is adopted in the LMS algorithm instead of the mean-square error value, i.e., $e(n)^2$ is used instead of $E[e(n)^2]$, so that the gradient estimation can be simplified, and as a result, the cost function becomes:

$$J(n) = \frac{1}{2} e(n)^2 \tag{5}$$

Eq. (5) is obtained by taking the first order partial derivative of $W(n)$, i.e., the gradient:

$$\frac{\partial J(n)}{\partial W(n)} = \left[e(n) \frac{\partial e(n)}{\partial w_0(n)}, e(n) \frac{\partial e(n)}{\partial w_1(n)}, \cdots e(n) \frac{\partial e(n)}{\partial w_{L-1}(n)} \right]^T = -e(n) X(n) \tag{6}$$

Therefore, the iterative formulation of the LMS algorithm is updated as:

$$W(n+1) = W(n) + \mu(-\nabla J(n)) = W(n) + \mu e(n) X(n) \tag{7}$$

where μ is the step size.

The adaptive filtering algorithm directly affects the performance of the adaptive filter. In the following, the performance of the LMS algorithm is analyzed in terms of convergence, convergence speed, steady state error, and computational complexity:

1) Algorithm convergence the adaptive filter weight coefficient error is defined as:

$$V(n) = W(n) - W_{opt}(n) \tag{8}$$

where $W(n)$ is the adaptive filter weight coefficient vector and $W_{opt}(n)$ is the optimal weight coefficient vector.

Deforming Eq. (8) by subtracting the optimal weight coefficient vector $W_{opt}(n)$ from both the left and right sides of the equation, Eq. (8) can be further changed to:

$$V(n+1) = V(n) + \mu e(n)X(n) \tag{9}$$

$e(n) = d(n) - y(n) = \xi(n) - X^T(n)V(n)$, where $\xi(n)$ is a Gaussian white noise with mean value 0. Assuming that $\xi(n)$ and the input signal vector $X(n)$ are independent of each other and have a mean value of 0, bringing $e(n)$ into Eq. (9) and taking the statistical expectation on both sides of Eq:

$$E\{V(n+1)\} = (I - \mu R)E\{V(n)\} \tag{10}$$

where R is the autocorrelation matrix of the input signal vector and can be decomposed as $R = QAQ^T$, since Q is a You matrix and A is a diagonal array consisting of all the eigenvalues of the autocorrelation matrix R.

Multiplying both sides of the equation (10) equation simultaneously left by Q^r, equation (10) becomes:

$$E\{Q^T V(n+1)\} = (I - \mu Q^T RQ)E\{Q^T V(n)\} \tag{11}$$

Eq. (11) can be obtained by deformation:

$$\begin{aligned} E\{Q^T V(n+1)\} &= (I - \mu\Lambda)E\{Q^T V(n)\} \\ &= \begin{bmatrix} 1-\mu\lambda_0 & 0 & \ldots & 0 \\ 0 & 1-\mu\lambda_1 & \ldots & 0 \\ \vdots & \vdots & \ddots & \vdots \\ 0 & 0 & \ldots & 1-\mu\lambda_{L-1} \end{bmatrix} E\{Q^T V(n)\} \end{aligned} \tag{12}$$

where L is the filter order.

Eq. (12) is obtained iteratively:

$$\begin{aligned} & E\{Q^T V(n+1)\} \\ &= \begin{bmatrix} (1-\mu\lambda_0)^{n+1} & 0 & \ldots & 0 \\ 0 & (1-\mu\lambda_1)^{n+1} & \ldots & 0 \\ \vdots & \vdots & \ddots & \vdots \\ 0 & 0 & \ldots & (1-\mu\lambda_L)^{n+1} \end{bmatrix} E\{Q^T V(0)\} \end{aligned} \tag{13}$$

From equation (13), the LMS algorithm convergence condition is:

$$-1 < 1 - \mu\lambda_{\max} < 1 \tag{14}$$

where $\lambda_{\max}$ is the maximum value of the eigenvalues of the autocorrelation matrix.

The range of values of the step size for convergence of the algorithm can be obtained from (14):

$$0 < \mu < \frac{2}{\lambda_{\max}} \tag{15}$$

However, a priori knowledge is still required for the step size selection, so the total power of the input signal, i.e., the trace of the autocorrelation matrix, is usually used instead of the eigenvalue maximum for the LMS algorithm, and Eq. (15) becomes:

$$0 < \mu < \frac{2}{tr[R]} \tag{16}$$

2) Convergence speed

When the weight coefficient error $E\{Q^T V(n+1)\}$ tends to 0, the weight coefficients $W(n)$ of the adaptive filter converge to the optimal solution $W_{opt}(n)$, during the convergence process, the weight coefficient error shows an exponential decrease, and the time-constant parameter is usually used to represent the speed of convergence, and the proportionality term of the n th component of the weight coefficient error is:

$$\gamma_n = 1 - \mu\lambda_n \tag{17}$$

The proportional term index declines and unfolds:

$$\gamma_n = e^{\frac{-1}{\tau_n}} = 1 - \frac{1}{\tau_n} + \frac{1}{2!\tau_n^2} + \ldots \tag{18}$$

where τ_n is the time constant, which is negligible in Eq. (18) because the time constant τ_n is so large that the higher terms tend to zero.

Joining the two equations (17) and (18), the time constant τ_n can be obtained as:

$$\tau_n \approx \frac{1}{\mu\lambda_n} \tag{19}$$

In the LMS algorithm, the rate of convergence of the algorithm is determined by the rate of convergence of one of the slowest converging weight coefficients, so the time constant takes the maximum value when λ_n takes the minimum value, which can be obtained as the time constant:

$$T = \tau_{\max} \approx \frac{1}{\mu\lambda_{\min}} \tag{20}$$

From Eq. (20), the maximum time constant is also governed by the step size, which is inversely proportional to the step size, in addition to being related to the minimum value of the eigenvalue. The maximum step size can be known from equation (13), and it can be obtained by bringing the maximum step size into equation (20):

$$T_{\min} = \frac{\lambda_{\max}}{2\lambda_{\min}} \tag{21}$$

From equation (21), it can be seen that the LMS algorithm obtains the minimum convergence time, i.e., the fastest convergence rate, by using the maximum theoretically convergent step size and the eigenvalues of the autocorrelation matrix are of the same value.

3) Steady state error

Since the solution derived using the fastest gradient descent method is suboptimal with respect to the Wiener solution, the algorithm does not result in a Wiener solution after convergence, but rather fluctuates in the region around the Wiener solution, with a steady-state error, which is often referred to as the steady-state excess mean square error (EMSE). Steady-state EMSE denotes the difference between the mean square error after the algorithm converges, as the iterative process of the algorithm continues, and after the steady state is reached, i.e., the difference between the steady state mean square error $MSE(\infty)$ after the LMS algorithm has converged and the minimum mean square error $MSE_{\min}$, with an EMSE of the form:

$$EMSE = tr[K(n)R] \tag{22}$$

where $K(n)$ is the weight coefficient error correlation matrix.

The steady state EMSE equation is:

$$EMSE = tr[K(+\infty)R] \tag{23}$$

For the LMS algorithm, the dislocation value is more indicative of the degree of deviation between the steady state value of the algorithm and the optimal solution, which is given by Eq:

$$M = \frac{EMSE}{MSE_{\min}} \tag{24}$$

The smaller the steady state EMSE value, the smaller the misalignment value M , the higher the accuracy of the convergence of the algorithm and the better the filter effect, but because of the use of the fastest descending gradient method, the resulting solution is not a Wiener solution, so the misalignment value M will never be 0. Usually, in practice, it is sufficient to take a misalignment value of 10% or less.

III. C. 2) Algorithm Performance Analysis

The APSA algorithm and the RLS algorithm are selected as the comparison algorithms, and the performance of the LMS algorithm is analyzed by simulation on the MATLAB platform, with the order of the filter M set to 30, and the length of the signal set to 3000. The flow of the algorithm performance analysis is as follows: firstly, a length of the random signal corresponding to the length of the signal is generated as the input signal with an ideal filter system, and then the input signal is added with a certain noise signal and the output of the ideal system is taken as the desired signal. Then the input signal is added with a certain noise signal, and the output of the ideal system is taken as the desired signal. A random system is then constructed and its coefficients are updated using three adaptive filtering algorithms, and the difference between the filter coefficients and the ideal filter coefficients is analyzed after each iteration to obtain the performance of the three algorithms. The number of iterations and the steady state error (NMSD) at convergence of different algorithms are assembled into a table, as shown in Table 1. The iteration speed of the RLS algorithm is significantly higher than the other two algorithms, the iteration speed of the LMS algorithm is slightly faster than that of the APSA algorithm, and the iteration speeds of all three algorithms show a decreasing trend with the increase of the mixing factor. However, the LMS algorithm outperforms the RLS algorithm and the APSA algorithm in terms of steady state error.Although the iteration speed of the LMS algorithm is slightly inferior to the RLS algorithm, the steady state error performance of the LMS algorithm is always optimal as the mixing factor increases, and it has a better performance overall.

Table 1: Algorithm Performance Comparison

Particle mixing coefficient	Iteration times			NMSD		
	LMS	RLS	APSA	LMS	RLS	APSA
0.5	2071	1265	2500	1.201	1.691	2.901
0.6	1650	1148	2355	0.73	0.787	2.123
0.7	1485	903	2008	0.13	0.113	1.514
0.8	1255	961	1773	-0.297	-0.785	0.88
0.9	1048	984	1878	-0.857	-1.473	0.363

IV. Spatial and temporal characterization of the coupling effect of the plateau vortex and atmospheric circulation

In this paper, we will use the relevant research data of the Tibetan Plateau from 1981 to 2024, and apply the identification method of plateau vortex, the calculation method of atmospheric heat source, and the LMS adaptive filtering algorithm to carry out the research on the spatial and temporal characterization of the coupling effect of the plateau vortex and the atmospheric circulation.

IV. A. Characterization of vortex generation in the high summer plateau

The number and distribution of the simulated July plateau vortex generation in 1985 (the year of high occurrence) and 2018 (the year of low occurrence) are specifically shown in Table 2.The number of plateau vortex generation simulated by the model in 1985 is lower than the statistics, and the number of plateau vortex generation simulated by the model in 2018 is basically the same as the statistics. The number of plateau vortex generation simulated by the model in 1985 is more than that in 2018. The model-simulated plateau vortices generated 16 plateau vortices west of 90°E, accounting for 80% of the total number of simulated vortices, which is basically consistent with the actual observed geographic distribution characteristics.

Table 2: Number of plateau vortex generation

Year	Plateau vortex data set	Modeling results	The number of simulated plateau vortexes west of 90 ° E
1985	22	14	16
2018	7	6	

IV. B. Comparative analysis of atmospheric circulation

According to the available research data, the 100hPa altitude in 1985 and 2018 shows that the South Asian high pressure center is westward, mainly located over the Iranian Plateau, and from the daily change of the 100hPa flow field, it can be found that the South Asian high pressure center ascends to the Tibetan Plateau at different times, and maintains over the Tibetan Plateau at different times: the South Asian high pressure center ascended to the Tibetan Plateau at 33hour in 1985, and maintained for 11 days, and the South Asian high pressure center ascended to the Tibetan Plateau at 34hour in 2018, and maintained for 11 days. 15 days, in 2018, the South Asian high pressure center mounted the Tibetan plateau in 34 Hou, maintaining the time of 11 days, with the previous statistics of more frequent years and fewer frequent years comparison results are roughly the same, more frequent years earlier than fewer frequent years mounted the Tibetan plateau, and maintained in the Tibetan plateau over a longer period of time. 100hPa relative vorticity of the daily changes in the specific as shown in Fig. 1, where the "doo The daily variation of 100hPa relative vorticity is shown in Fig. 1, in which "duo" stands for more frequent years and "shao" stands for less frequent years. It can be seen that the high altitude in June of the most frequent year shows negative vorticity, and the less frequent year is positive vorticity at 32-33 Hou.

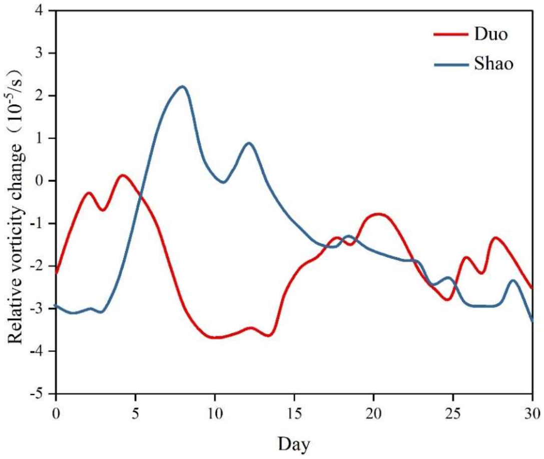

Figure 1" Diurnal variation of relative vorticity at 100 hPa(80-100°E,28-34°N)

The values of ground sensible heat, latent heat and heat source in the Tibetan Plateau are shown in Table 3. In the table, Q_H is the ground sensible heat flux, Q_E is the ground latent heat flux, and Q_H+Q_E is the ground heat source. From the table, it can be seen that the Tibetan Plateau is the heat source, with an average of more than 115 w/m², which is slightly stronger in the most frequent years, which may be one of the reasons for the high pressure center of South Asia to be located over the Tibetan Plateau on a larger number of days. The surface sensible heat value is nearly twice as much as the latent heat value, indicating that the sensible heat contribution to the surface heat flux is greater in June.

Table 3: Ground sensible heat, latent heat and heat source value

Year	Q_H(w/m²)	Q_E(w/m²)	Q_H+Q_E(w/m²)
1985	77.4	41.2	119.6
2018	74.3	38.6	115.9

The daily changes of ground heat source, sensible heat and latent heat in the Tibetan Plateau are specifically shown in Fig. 2, and Figs. (a) to (c) correspond to ground heat source, ground sensible heat and ground latent heat, respectively. The ground heat source showed an increasing trend in June, and the heat source in the more frequent year has been stronger than that in the less frequent year. In the first 3 Hou, the ground sensible heat is stronger and shows an increasing trend. And the heat sensing strengthens the convergence of the low-level airflow, which enhances the upward movement, thus affecting the high-level circulation. It can be seen that 32, 33 Hou more hairy years and less hairy year difference is larger, after 3 Hou, the ground heat sensing decreases, and the gap between more hairy years and less hairy years decreases. Compared with the daily change of relative vorticity at 100hPa, the trend of the two changes is more or less the same. 32 and 33 Hou, the heat sensibility of the most common year is strong, and the upper air is negative vorticity, while the heat sensibility of the less common year at this time is the lowest in the month, and it is positive vorticity. after 33 Hou, the heat sensibility of the most common year decreases, the negative vorticity is weakened, the heat sensibility of the less common year increases compared with that of 32-33 Hou, and the upper air is negative vorticity and is continuously strengthening, and the heat sensibility of the most common year and the least common year is more and more negative. The difference between the heat sensing value of the prevalent year and the less prevalent year decreases, and the relative vorticity values are close to each other. This indicates that there is a certain connection between the surface heat flux and the atmospheric circulation. The latent heat of the ground decreases in the first three chambers of the prevalent year and increases in the last three chambers, while the latent heat of the ground increases and then decreases in the first three chambers of the prevalent year and continues to increase in the last three chambers. Overall, the sensible heat value is larger than the latent heat, and the total contribution is larger.

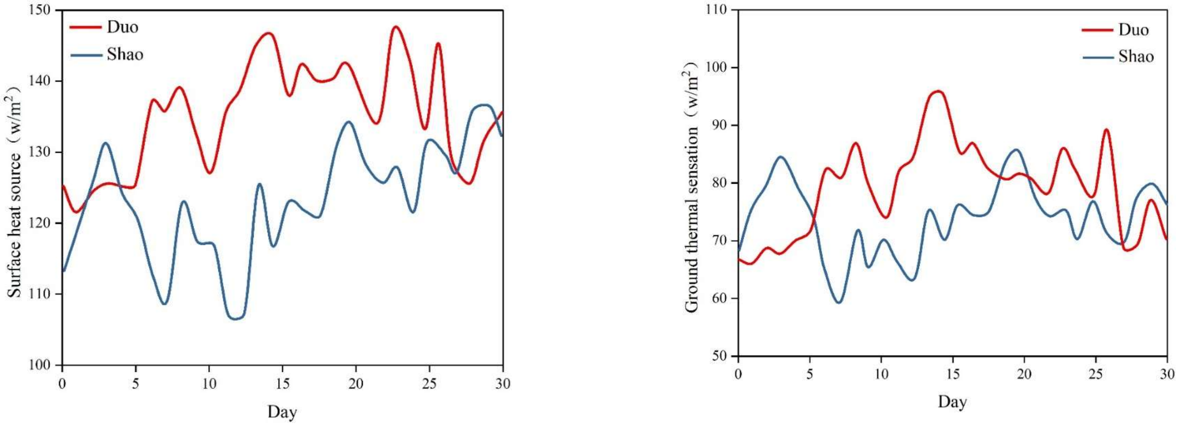

(a)Ground heat source

(b)Sensible heat

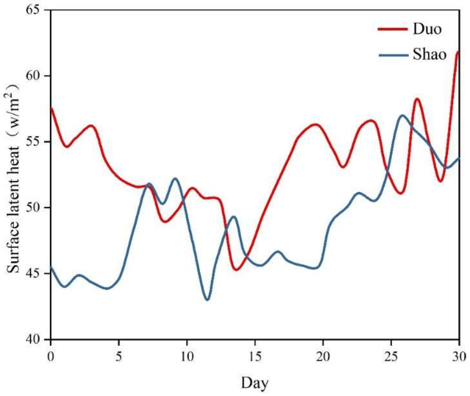

(c)Latent heat day

Figure 2: The change of ground heat source, sensible heat and latent heat day

IV. C. Characteristics of the spatial and temporal distribution of the climatic state of the plateau low vortex

IV. C. 1) Characteristics of the temporal distribution of the climatic state of the plateau low vortex

The time series of the annual average number of plateau vortices generated by the three sets of reanalyzed data, MERRA-2, ERA-Interim, and JRA55, and the results of the linear fitting are shown in Figure 3. The average number of low vortices generated by the three sets of data is about 65 per year, of which the annual average of MERRA-2 data is 65.43, the annual average of ERA-Interim is 64.22, and the annual average of JRA55 is 65.08, which is not much different from each other. The standard deviation of JRA55 is the largest among the three data sets and has the strongest interannual variability, followed by MERRA-2, and ERA-Interim is the smallest. In addition we calculated the correlation coefficients between the three sets of information. The highest correlation coefficient between MERRA-2 and ERA-Interim was 0.58, which exceeded the 99.9% confidence test, and the correlation coefficient between JRA55 and the other two sets of information was 0.45, which exceeded the 99% confidence test. In addition, the results of the linear fits of all three sets of data indicate an increasing trend in the number of low vortices generated on the plateau, with similar results for MERRA-2 and ERAInterim: an increase in the annual mean number of low vortices by about 2 per decade, and a slightly lesser result for JRA55, with an increase of about 1 per decade.

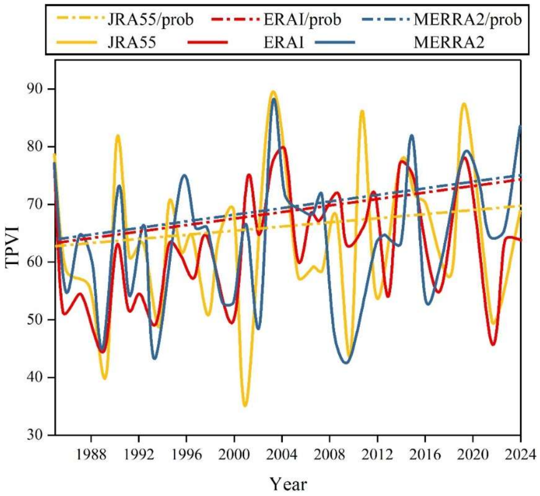

Figure 3: Time series and linear fitting of annual average number of plateau vortexes

In addition to the significant interannual variability, the number of generated low vortices in the plateau is characterized by a typical annual cycle, as shown in Fig. 4. Figures (a) and (b) show the distribution of the number of plateau low vortices in different months of the three sets of data, and the distribution of the number of low vortices in April-September of each year from 1985-2018 of the MERRA-2 reanalysis data, respectively. From the perspective of annual cycle, the frequency of plateau vortex generation is characterized by a significant warm season. All three sets of data reflect the summer unimodal nature. The warm season (May-September) generates more than 75% of the plateau vortices in the whole year, among which the JRA55 and MERRA-2 data have the highest number of vortices generated in July, and the ERA-Interim data have the highest number of vortices generated in June. There are also significant interannual variations in the number of vortices generated in each month, with the standard deviation of the number of vortices generated in July being the largest in ERA-Interim and JRA55, and in September in MERRA-2, with the standard deviation of the number of vortices generated in July being comparable to that of August. In addition, the time-series correlation of the number of vortices generated in each month is not good, that is to say, the large-scale circulation background can only partially explain the reasons for the number of vortices generated.

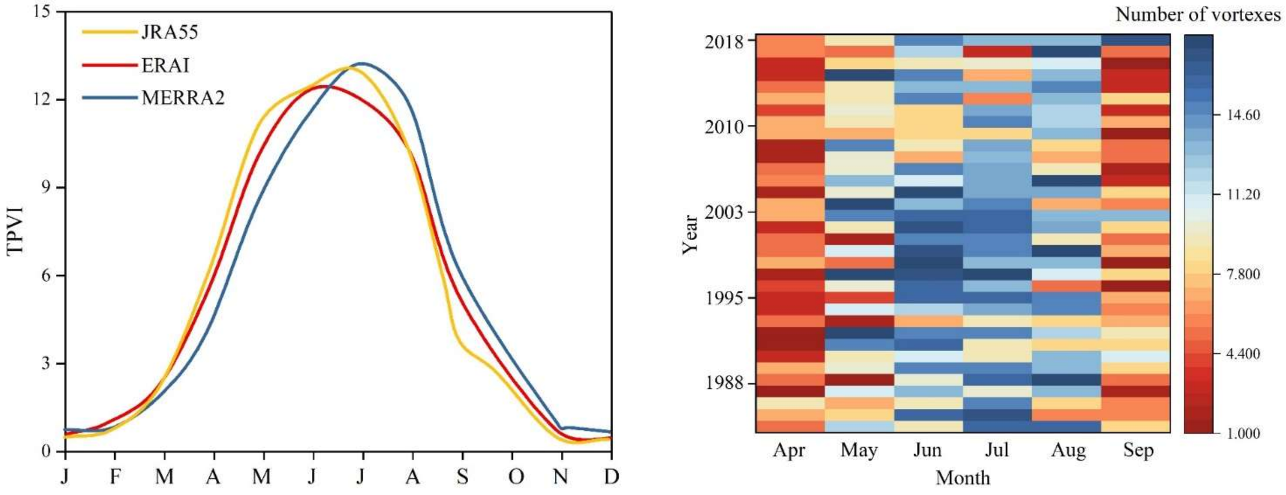

(a)The number of plateau vortexes in different months

(b)The number distribution of low vortex from April to September

Figure 4: The annual cycle characteristics of the number of plateau vortexes

IV. C. 2) Characteristics of the spatial distribution of the climatic state of the plateau low vortex

In this section, the spatial distribution characteristics of the location of the low vortex generation will be explored. The variation of the number of low vortex generation with longitude in summer months is shown in Fig. 5, Fig. (a) shows the evolution sequence of the number of low vortex generation on the plateau with longitude in June, July and August, and Fig. (b) shows the evolution sequence of the number of low vortex generation on the plateau with latitude in June, July and August. The number of low vortex generation increases steeply at 80°E, and the location with the most low vortex generation is located near 82°E, which can be more than 26 vortices, and decreases gradually west of 90°E. The distribution of low vortex generation locations in July is similar to that in June, but the proportion of low vortex generation in the eastern part of the country has increased, and the location with the most vortex generation is located near 85°E, which is shifted to the east a little bit, and the number of vortices generated near Mt. There is a slight eastward shift, and the number of low vortices generated near the Gondwana Mountains increases, while few low vortices are generated east of 95°E.

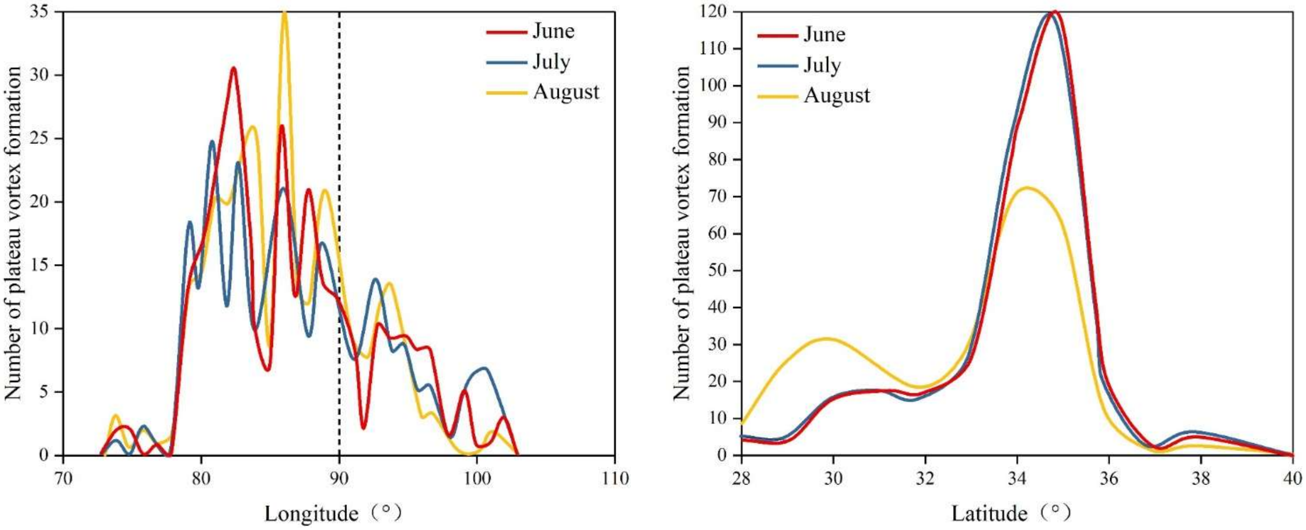

(a)Evolution sequence of the number of plateau vortexes with longitude

(b)Evolution sequence of the number of plateau vortex generation with latitude

Figure 5: Spatial distribution characteristics of the low vortex generation position

V. Conclusion

This study reveals the coupling effect between the plateau vortex and the atmospheric circulation by analyzing the generation characteristics of the plateau vortex in 1985 and 2018. The results show that the generation of plateau eddies is closely related to the surface heat source on the Tibetan Plateau. The number of plateau eddies generated in 1985 was 22, while that of 2018 was 7, indicating that there is a significant difference in the generation of eddies between the years of multiple and fewer occurrences. By calculating the ground sensible heat, latent heat and heat source values, it is found that the intensity of the heat source on the Tibetan Plateau is stronger in 1985 than in 2018 for the multiple-occurrence year, and the ground sensible heat value has a more prominent effect on the vortex activity. Specifically, the higher ground sensible heat value in the occurrence year promotes the upward movement of the airflow, which in turn contributes to the vortex generation at high altitudes. In contrast, the lower ground sensible heat values in the less frequent years resulted in a lower frequency of vortex generation in the plateau.

In addition, the study also shows that the activity of the South Asian high pressure center has a significant moderating effect on the generation of plateau vortices, especially in the warm season, when the influence of the South Asian high pressure is enhanced, further promoting the generation of plateau vortices. The feedback effect of the change of the surface heat source on the atmospheric circulation also plays a key role in the vortex generation process.

In summary, the coupling effect between the plateau vortex and the atmospheric circulation is complex, but the changes of the ground heat source, especially the sensible heat flux, have a direct influence on the generation of the plateau vortex.

References

[1] Yan, H., Huang, J., He, Y., Liu, Y., Wang, T., & Li, J. (2020). Atmospheric water vapor budget and its long-term trend over the Tibetan Plateau. Journal of Geophysical Research: Atmospheres, 125(23), e2020JD033297.

[2] Sun, C., Xu, X., Zhao, T., Yao, T., Zhang, D., Wang, N., ... & Cai, W. (2022). Distinct impacts of vapor transport from the tropical oceans on the regional glacier retreat over the Qinghai-Tibet Plateau. Science of the Total Environment, 823, 153545.

[3] Zhang, F., Wang, C., & Pu, Z. (2019). Genesis of Tibetan Plateau vortex: Roles of surface diabatic and atmospheric condensational latent heating. Journal of Applied Meteorology and Climatology, 58(12), 2633-2651.

[4] Zhang, K., Wu, Y., Wang, F., Li, X., Cui, S., Zhang, Z., ... & Huang, Y. (2022). Characteristics of the vertical structure of the atmospheric turbulence in the Tibetan Plateau. Science China Earth Sciences, 65(7), 1368-1378.

[5] Liao, Q., Li, X., Shi, F., Deng, Y., Wang, P., Wu, T., ... & Zuo, F. (2022). Diurnal evapotranspiration and its controlling factors of Alpine ecosystems during the growing season in northeast qinghai-tibet plateau. Water, 14(5), 700.

[6] Chen, J., Wen, J., Kang, S., Meng, X., Tian, H., Ma, X., & Yuan, Y. (2020). Assessments of the factors controlling latent heat flux and the coupling degree between an alpine wetland and the atmosphere on the Qinghai-Tibetan Plateau in summer. Atmospheric Research, 240, 104937.

[7] Huang, W., Cheng, B., Zhang, J., Zhang, Z., Vihma, T., Li, Z., & Niu, F. (2019). Modeling experiments on seasonal lake ice mass and energy balance in the Qinghai–Tibet Plateau: a case study. Hydrology and Earth System Sciences, 23(4), 2173-2186.

[8] Meng, D., Dong, Q., Kong, F., Yin, Z., Li, Y., & Liu, J. (2020). Spatio-temporal variations of water vapor budget over the Tibetan Plateau in summer and its relationship with the Indo-Pacific warm pool. Atmosphere, 11(8), 828.

[9] Li, M., Wang, L., Chang, N., Gong, M., Ma, Y., Yang, Y., ... & Sun, F. (2021). Characteristics of the water vapor transport in the canyon area of the southeastern Tibetan Plateau. Water, 13(24), 3620.

[10] Shi, F., Li, X., Zhao, S., Ma, Y., Wei, J., Liao, Q., & Chen, D. (2024). Evaporation and sublimation measurement and modeling of an alpine saline lake influenced by freeze–thaw on the Qinghai–Tibet Plateau. Hydrology and Earth System Sciences, 28(1), 163-178.

[11] Cao, S., Cao, G., Chen, K., Han, G., Liu, Y., Yang, Y., & Li, X. (2019). Characteristics of CO2, water vapor, and energy exchanges at a headwater wetland ecosystem of the Qinghai Lake. Canadian Journal of Soil Science, 99(3), 227-243.

[12] Ma, Q., Zhang, C., Wang, D., & Pang, Z. (2024). Summer Atmospheric Water Cycle under the Transition Influence of the Westerly and Summer Monsoon over the Yarlung Zangbo River Basin in the Southern Tibetan Plateau. Advances in Atmospheric Sciences, 41(5), 830-846.

[13] Liu, Y., Lu, M., Yang, H., Duan, A., He, B., Yang, S., & Wu, G. (2020). Land–atmosphere–ocean coupling associated with the Tibetan Plateau and its climate impacts. National Science Review, 7(3), 534-552.

[14] Huang, J., Zhou, X., Wu, G., Xu, X., Zhao, Q., Liu, Y., ... & Qie, K. (2023). Global climate impacts of land-surface and atmospheric processes over the Tibetan Plateau. Reviews of Geophysics, 61(3), e2022RG000771.

[15] M. Raja,P. Hasan,Md. Mahmudunnobe,Md. Saifuddin & S.N. Hasan. (2024). Membership determination in open clusters using the DBSCAN Clustering Algorithm. Astronomy and Computing,47,100826-.

[16] Daniel G. Tiglea,Renato Candido & Magno T.M. Silva. (2025). Bias-Variance Decomposition of the Mean-Square Deviation of the LMS Algorithm: Transient and Steady-State Analysis. Circuits, Systems, and Signal Processing,44(6),1-32.

[17] Tejaswini A. Bhosale & S. Pushkar. (2024). IWF-ECTIC: Improved Wiener filtering and ensemble of classification model for tourism image classification. Multimedia Tools and Applications,(prepublish),1-38.